FAKULTÄT FÜR PHYSIK
Institut für Theoretische Physik

NLO QCD corrections for ZH and ZH+jet production at the LHC

Diplomarbeit
von

Michael Schüßler

am Institut für Theoretische Physik

Referent: Prof. Dr. D. Zeppenfeld
Korreferent: PD Dr. S. Gieseke

Bearbeitungszeit: 01.04.2016 – 17.03.2017

Erklärung zur Selbstständigkeit

Ich versichere, dass ich diese Arbeit selbstständig verfasst habe und keine anderen als die angegebenen Quellen und Hilfsmittel benutzt habe, die wörtlich oder inhaltlich übernommenen Stellen als solche kenntlich gemacht und die Satzung des KIT zur Sicherung guter wissenschaftlicher Praxis in der gültigen Fassung vom 17.05.2010 beachtet habe.

Karlsruhe, den 17.03.2017, _____

Michael Schüßler

Als Ansichtsexemplar genehmigt von

Karlsruhe, den 17.03.2017, _____

Prof. Dr. D. Zeppenfeld

Contents

1. Introduction

The task of a physicist is to analyze and to describe the elementary principles of the universe. He or she is then to model those interactions in an illustrative form that allows for predictions and provides a general understanding of the moving parts of nature. Those insights should later become a resource for other professions, like chemistry, engineering and even philosophy, to improve the comprehension of their respective fields. The spectrum of physics phenomena ranges from the investigation of the large scale motions of astral bodies down to the microscopic interaction between two pointlike particles.

This very broad range of investigated scales is also represented in the current models that describe it. The movement of celestial objects are described by General Relativity, a theory, that derives the laws of gravity from the geometry of space time itself. At the other end of the spectrum lies the Standard Model. It describes the elementary building blocks of matter and the forces acting between them. Although the Standard Model was conceived during the second half of the last century, it describes experimental data to this day with tremendous accuracy.

There are evident phenomena, like the nature of dark matter and dark energy, explained by neither of the above theories. And even within their respective frames of reference, there are unexplained discrepancies. The very accurately measured quantity of the muon g-factor, for example, depicts a statistically significant deviation from the theoretical Standard Model prediction. One has also so far not been able to combine both models to form one unified theory. A cynic might say, those models are obviously wrong. But one can also think about them as effective models describing a scale separated subset of problems.

The 300 year old description of gravity by Isaac Newton is still completely sufficient for the structural analysis of buildings. On the contrary, the incorporation of special or general relativity into statics would be a grave mistake. As chemistry did not get obsolete with the formulation of quantum mechanics. And quantum mechanics survived the conception of quantum field theory. The standard model will never completely be replaced by the next, more precise model.

Many theoretical predictions of the Standard Model are approximations, often calculated numerically. And even the analytical results often need to be evaluated computationally because they are represented by long and complex mathematical expressions. To find new models, one has to analyze deviations of experimental data from the current predictions. The most profitable tools for probing elemental particle interactions are collider experiments. To find discrepancies from the established model, one can move in two different directions. One could increase the energy scale of the experiments to reach a region where the effective approximation of the current model breaks down. Or one could increase the accuracy of the predictions at the current scale to make smaller variations visible.

The highest energy collision experiment currently running is the Large Hadron Collider in Cern, Switzerland. The experiment has accumulated a vast amount of experimental

data over the last decade leading to the 2012 discovery [1] [2] of the Higgs boson, the last Standard Model particle of which experimental verification was missing. Since then no major discoveries have been published. As the next big particle experiment is probably years from being realized, precision calculations seem to be the key to unlocking new physics. The basis for these more accurate predictions is technically restricted by available computational power. In this sector development of higher frequency and higher transistor count computer chips has stagnated a in recent years. And a clear trend of increasing computational speed by using multiple CPUs has emerged. With this in mind, easily parallelizable calculations are at an advantage.

Computational tools of this kind are Monte Carlo simulations. The assignment of this diploma thesis was the extension of the Monte Carlo program VBFNLO [3] , a software focused on providing model predictions for the Large Hadron Collider experiment. For this task two Standard Model processes were added to the program.

2. Theoretical Background

This chapter presents a short overview of the theoretical basis of the master thesis. We start with a brief introduction of the standard model decomposed into its two interaction sectors. After that, particle collider experiments and the related concept of cross sections are introduced. In the following section we discuss the calculation of scattering matrix elements at different orders of perturbation theory. The last two sections of the chapter are devoted to the discussion of parton distribution functions and the method of Monte Carlo integration. A lot of the notation in this chapter is taken from the textbook "Introduction to Quantum Field Theory" [4] by M. Peskin and D. Schroeder, that I can highly recommend.

2.1 The Standard Model

The standard model is a relativistic quantum field theory, it combines elements of classical field theory together with the realizations of quantum mechanics to a consistent theory that incorporates the principles of Einstein's theory of special relativity.

For the remainder of the thesis, we will abbreviate the Standard Model with "SM". It describes three of the four elementary interactions of nature: the strong, the electromagnetic and the weak interaction. In the SM matter particles appear as fermionic operator fields and interactions are mediated by bosonic ones. The dynamics of all appearing fields follow from the Lagrangian density $\mathcal{L}$ via the principle of least action.

The SM is also a gauge theory which denotes the fact that the Lagrangian $\mathcal{L}$ is invariant under a continuous group of local transformations, called gauge transformations. The total gauge symmetry group of the SM is $SU(3) \times SU(2) \times U(1)$, denoting the direct product of special unitary and unitary Lie groups. The strong interaction falls under the symmetry group $SU(3)$ and the theory describing it is called Quantum Chromodynamics, short QCD. The remaining weak and electromagnetic forces obey the $SU(2) \times U(1)$ symmetry and have been combined into the electroweak (EW) interaction. These two building blocks of the SM will be described in further detail in the following sections.

2.1.1 Quantum Chromo Dynamics

This part of the SM describes the strong interaction and the fermions it acts upon. It is the force that corresponds to the non-abelian color gauge Group $SU(3)_C$. The massive fermions of QCD are called quarks and live in the fundamental **3** representation of the gauge group resulting in 3 colors and 3 anticolors. The gauge bosons of the interaction are named gluons and lie in the adjoint representation **8** of the group, amounting to 8 different color states. The gluon charges can be described by a pair of a color and an anticolor in the quark color space. The QCD lagrangian has the following form:

$$\mathcal{L}_{QCD} = \bar{\psi}_j (i\gamma^\mu D_\mu)_{jk} - m\delta_{jk})\psi_k - \frac{1}{4} G^a_{\mu\nu} G^{\mu\nu}_a \tag{2.1}$$

with ψ denoting a Dirac spinor, j, k the quark colors and a the gluon color index. D_μ refers to the covariant derivative and $G^a_{\mu\nu}$ is the gluon field strength tensor:

$$D_\mu = \partial_\mu - igA^a_\mu \lambda_a, \quad G^a_{\mu\nu} = \partial_\mu A^a_\nu - \partial_\nu A^a_\mu + g_s f^{abc} A^b_\mu A^c_\nu \tag{2.2}$$

Here f^{abc} are the structure constants of the $SU(3)_C$ group and λ_a are the Gell-Mann matrices. Through the term in the Lagrangian containing the covariant derivative the coupling of the quarks to the gluon field A^a_μ is introduced: The strong interaction between quarks is mediated by gluons.

Quarks appear in three generations, each consisting of an up-type and an down-type quark. The two quark types differ from each other through their different couplings to the electroweak sector. The quarks generations are named: up and down, charm and strange, top and bottom.

2.1.2 Electroweak Interaction

The electroweak sector of the standard model unifies the electromagnetic and the weak interaction and corresponds to the gauge symmetry group $SU(2)_L \times U(1)_Y$. This revolutionary step was conceived by S. Glashow, A. Salam and S. Weinberg [5] [6] [7] .

In the EW Lagrangian an additional type of matter fermions, called leptons appear. They also constitute three generations, consisting of a pair of a lepton l and a lepton neutrino ν each. The leptons are named electron, muon and tau. Before spontaneous symmetry breaking the EW Lagrangian can be discribed by the following Lagrangian

$$\mathcal{L}_{EW} = \mathcal{L}_{Fermions} + \mathcal{L}_{Bosons} + \mathcal{L}_{Higgs} + \mathcal{L}_{Yukawa} \tag{2.3}$$

To the fermion term the matter particles appear in left-handed $SU(2)_L$ doublets and right-handed singlets with j denoting their generation:

$$Q_j = \begin{pmatrix} u_j \\ d_j \end{pmatrix}_{l.h.}, \quad E = \begin{pmatrix} l_j \\ \nu_j \end{pmatrix}_{l.h.}, \quad u_j = u_{j|r.h.}, \quad d_j = d_{j|r.h.}, \quad l_j = l_{j|r.h.} \tag{2.4}$$

$$\mathcal{L}_{Fermions} = \sum_{L=Q_j,E_j} \bar{L} i\gamma^\mu D_\mu L + \sum_{r=u_j,d_j,l_j} \bar{r} i\gamma^\mu D_\mu r \tag{2.5}$$

$$D_\mu = \partial_\mu - igW^a_\mu \frac{\sigma_a}{2} - ig'YB_\mu \tag{2.6}$$

The W^a_μ are the three gauge fields of the $SU(2)_L$ group and they only couple to left-handed doublets. B_μ is the field of $U(1)_Y$. A mass Term of the form $-m\bar{\psi}\psi$ as we encountered in QCD is not possible here, because it is not invariant under $SU(2)_L$ gauge transformations. The boson term is just the familiar:

$$\mathcal{L}_{Bosons} = -\frac{1}{4} W^a_{\mu\nu} W^{\mu\nu}_a - \frac{1}{4} B_{\mu\nu} B^{\mu\nu} \tag{2.7}$$

In L_{Higgs} an additional scalar $SU(2)_L$ field ϕ is introduced:

$$L_{Higgs} = |D_\mu \phi|^2 + \mu^2 \phi^\dagger \phi - \lambda(\phi^\dagger \phi)^2, \quad \phi = \frac{1}{\sqrt{2}} \begin{pmatrix} \phi^+ \\ \phi_0 \end{pmatrix} \tag{2.8}$$

2.1.3 Spontaneous Symmetry Breaking

In a preparational step we use the available gauge symmetry to let first Higgs field component ϕ^+ vanish and to make the second component ϕ^0 real. With $\mu^2, \lambda > 0$ the potential energy in the Higgs Lagrangian then becomes minimal for $\phi^0 = \sqrt{\mu^2/\lambda} =: v$. Next, the Higgs field is redefined around that minimum $h(x) = \phi^0 - v$. The procedure is summarized in the following equation:

$$\phi(x) = \frac{1}{\sqrt{2}} \begin{pmatrix} \phi^+ \\ \phi_0 \end{pmatrix} \quad \Rightarrow \quad \phi(x) = \frac{1}{\sqrt{2}} \begin{pmatrix} 0 \\ \phi_0 \end{pmatrix} =: \frac{1}{\sqrt{2}} \begin{pmatrix} 0 \\ v + h(x) \end{pmatrix} \tag{2.9}$$

With this redefinition we can rewrite the complete SM Lagrangian depending on the scalar Higgs field h. The kinetic term of the EW sector then looks like this:

$$\mathcal{L}_{kin} = \sum_f \bar{\psi}_f(\gamma^\mu \partial_\mu - m_f)\psi_f - \frac{1}{2} W^+_{\mu\nu} W^{-\mu\nu} + m_W^2 W^+_\mu W^{-\mu} - \frac{1}{4} Z_{\mu\nu} Z^{\mu\nu} \tag{2.10}$$

$$+ \frac{1}{2} m_Z^2 Z_\mu Z^\mu - \frac{1}{4} A_{\mu\nu} A^{\mu\nu} + \frac{1}{2}(\partial^\mu h)(\partial_\mu h) - \frac{1}{2} m_h^2 h^2 \tag{2.11}$$

To arrive at the above description, the EW gauge bosons have to be redefined in the following way. The occurring angle $\theta_w = sin^{-1}(g'/\sqrt{g^2 + g'^2})$ is called Weinberg angle:

$$W^\pm = \frac{1}{2}(W^1_\mu \mp i W^2_\mu), \quad \begin{pmatrix} Z_\mu \\ A_\mu \end{pmatrix} = \begin{pmatrix} cos\theta_w & -sin\theta_w \\ sin\theta_w & cos\theta_w \end{pmatrix} \begin{pmatrix} W^3_\mu \\ B_\mu \end{pmatrix} \tag{2.12}$$

These representations of the EW gauge bosons are called their mass eigenstates, because it matches the experimental observations of two massive charged gauge bosons W^+, W^- and two neutral bosons Z and A. Of which the photon A, also often denoted γ, is massless.

In equation 2.10 we saw that the gauge bosons and the fermions gained masses through the Higgs field obtaining a non-zero vacuum expectation value v. This principle is called the Higgs mechanism and was invented R. Brout, F. Englert and P. Higgs [8] [9] [10] . The Lagrangian with the appearing mass terms is also no longer invariant under the $SU(2)_L$ gauge symmetry. This process is called spontaneous symmetry breaking.

The resulting masses are as follows:

$$m_W = \frac{1}{2} g v, \quad m_Z = \frac{1}{cos\theta_w} m_W, \quad m_h = \sqrt{2\lambda} v \tag{2.13}$$

2.2 Particle Physics Experiments

The most successful experiments for the examination of elementary particle interactions are particle colliders. In those experiments a beam of accelerated particles is either shot against a fixed target or two beams are aimed at each other forcing the accelerated particles into high speed collisions. The very high rest frame energy in those collisions allows for the creation of heavy particles that are unobsoverable at the natural energy levels occurring on earth.

Every collision produces multitude of high speed particles perpendicular to the beam axis. The detector of the experiment then tries to identify those particles and to measure there momenta and energies. Different types of particles are registered in different parts of the

detector specifically designed for that purpose. This set of produced particles is referred to as a production event in the language of high energy physics.

For each type of event there are numerous SM processes that result in the production of the identified final state particles. The rate, at which an event of that type is supposed to occur, can be calculated from SM principles and later compared to the recorded experimental data. The typical quantity that measures the frequency with which a process occurs is a collider experiment is called a cross section.

2.3 Cross Sections

The cross section σ is defined as the production rate $\mathcal{N}$ of the event times the beam area A divided by the rate of pair collisions in that area. This definition allows for direct comparison between experiments with different beam geometries. In reality the beams are not continuous and the particles collide in bunches. If N particles are contained in each one and pairs of bunches collidide with a frequency ν, the cross section can be estimated to:

$$\sigma = \frac{\mathcal{N}A}{\mathcal{N}_{col.}} = \frac{\mathcal{N}A}{N^2\nu} \tag{2.14}$$

Cross sections are usually specified in units of *barns*, with $1b = 10^{-28}m^2$ being a unit of area.

From the theory side, cross sections can be calculated from a scattering matrix element $\langle\{p_f\}|S|p_a p_b\rangle$ with the scattering matrix S. p_a, p_b are the momenta of the two scattering beam particles and p_f those of the final state particles produced in the collision. With this the cross section can be represented by:

$$\sigma = \frac{1}{2E_{com}} \prod_f \left[\int \frac{d^3p_f}{(2\pi)^3 2E_f} \right] |\langle\{p_f\}|S|p_a p_b\rangle|^2 (2\pi)^4 \delta^{(4)}(\sum_f p_f - p_a - p_b) \tag{2.15}$$

Here E_{com} is the center of mass energy of the collision. The scattering matrix elements can be calculated from SM principles. This is usually done in an approximation by a finite perturbative expansion of the matrix element.

2.4 Perturbative Expansion

In particle physics, matrix elements, like the one appearing in the previous section, are usually evaluated in a perturbative expansion series. In this expansion, the interactions from the Lagrangian appear in orders of dimensionless coupling constants $\alpha_s = g_s^2/(4\pi)$ for the QCD and $\alpha = (gg')^2/[4\pi(g^2 + g'^2)]$ for the EW sector. If the couplings are significantly smaller then one, the series converges quickly and the exact matrix element can be approximated by a finite amount of low order terms.

These terms can be decomposed into integrals over products of two-point correlation functions named propagators. These integrals can be visually illustrated by so called Feynman diagrams. In these diagrams propagators are drawn as lines which are connected at verteces that represent the local interactions of the fields in the Lagrangian. External particles appear as legs leading out of those diagrams.

2.4.1 LO calculations

For each collider physics process there is a minimum occurrence of couplings needed to produce the characteristic final state particles. The order of the perturbation series at which those minimal couplings appear is called leading-order or short "LO". LO diagrams contain no closed circuits of propagators, which are called loops in the language of Feynman diagrams. If a loop was contained in a LO diagram, there would be a part of the loop where a propagator could be removed producing a different diagram for the same process. That diagram would be of a lower order resulting in a contradiction.

Because of the tree structure of LO diagrams, the momenta of all internal particles are fixed by those of the external particles since momentum is conserved at each vertex.

As an example of LO diagrams, they are shown in figure 2.1 for the three dominant Higgs production channels in hadron-hadron-collisions.

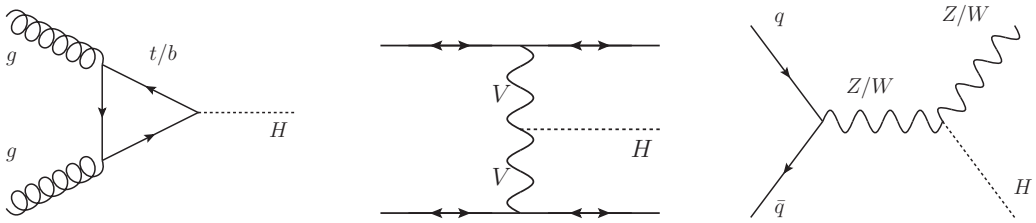

a) gluon fusion b) vector boson fusion c) Higgs-strahlung

Figure 2.1: Main Higgs production channels

2.4.2 NLO calculations

If you increase the order of the couplings by one, the new terms of the expansion are called next-to-leading-order (NLO) terms. The order after that is termed NNLO and so forth. NLO terms can be split into two categaories: Contributions in which the extra coupling leads to an additional external particle, these are called real emissions. And contributions, where the extra coupling introduces a loop into the calculation.

We are only considering NLO terms of the QCD coupling α_s in this thesis. They represent much bigger corrections to the LO calculation compared to their EW counterparts, because $\alpha_s/\alpha > 10$ at typical scales.

2.4.3 Virtual Corrections

Loops introduce an integral over an unconstrained loop momentum q into the calculation. This leads to the introduction of two types of divergencies. Ultraviolet divergencies result from the actuality that there is no upper bound on the absolute value of the loop momentum. Therefore the diagram becomes infinite, when we naively integrate over internal momenta. A physical cross section is of course finite. This implies that at least the sum of all contributions of our perturbative expansion has to become finite, or the method itself would not applicable.

The procedure of making individual diagrams finite without changing the sum of all contributions is called regularization. In the most common variant, called dimensional regularization, the integral is calculated in $4 - 2\varepsilon$ dimensions instead of four. With $\varepsilon > 0$ the integral converges to a sum of finite terms and expressions depending on ε. When all the NLO loop diagrams are summed, the ε-dependent terms cancel against each other, yielding a finite result.

The systematic treatment and classification of occurring divergencies is called the theory of renormalization. Through renormalization a finite theory of interactions can be reconstructed by adjusting field theory parameters in the in the Lagrangian and the introduction of countertems that contain the divergent structure. With this renormalized lagrangian a perturbative expansion can be realized yielding only ultraviolet finite diagrams. The fixing of the renormalized parameters introduces a new degree of freedom, the renormalization scale μ_R. This mechanic highlights a physical phenomenon, called the running of α_s. The renormalized value of α_s at NLO taken from [4] is:

$$\alpha_s(\mu_R^2) = \frac{4\pi}{b_0 \; ln(\mu_R^2/\Lambda_{QCD}^2)}, \quad b_0 = 11 - 2/3 n_f \tag{2.16}$$

Here Λ_{QCD} describes the approximate scale at which the coupling α_s becomes large and perturbation theory breaks down, it is experimentally estimated to a value of around $\Lambda_{QCD} \approx 200 MeV$; n_f is the number of approximately massless quark flavors in the theory.

Because the QCD coupling α_s is large at low energy scales, quarks form very stable bound states called hadrons. Which also explains why no free quarks can be observed at natural energy levels. On the other hand the coupling becomes weak in the high energy regime that is produced in particle colliders, allowing us to describe those "hard" interactions in the framework of perturbation theory.

The second type of divergencies, mentioned at the beginning of the section, are called infrared divergencies. Since the loop momentum q is integrated over the whole of momentum space, it also includes the region where the denominator of the propagator of a massless loop particle becomes zero. This infrared divergence is usually treated by dimensional regularization as well. Unfortunately it is not compensated by contributions of other virtual diagrams as happened in the ultraviolet case. It cancels against the divergencies appearing in the real emission diagrams instead.

2.5 Parton Distirbution Functions

To make predictions for the Large Hadron Collider experiment, or LHC, a description for hadron-hadron-collision cross sections is needed. Since the low energy "soft" physics of the hadron bound states can not be described by perturbation theory, an alternative approach has to be applied. It comes in the form of parton distribution functions $f_i(x, \mu_F)$ for each of the different QCD particles i. They can be interpreted as the probability of finding a parton i with a fraction x of the hadron momentum $p_i = x p_{had.}$ when probed at the scale μ_F. From this interpretation, basic attributes of the PDFs can be derived:

$$\sum_i \int_0^1 dx \; x f_i(x, \mu_F) = 1; \quad \int_0^1 dx \; f_q(x, \mu_F) - f_{\bar{q}}(x, \mu_F) = n_q \quad , \mu_F \to 0 \tag{2.17}$$

The first equation describes that the full momentum of the hadron has to regained when summing over all contributions. The second equation depicts, that PDFs should represent hadron constituents in the low scale limit. In the example of the proton this would refer to $n_{up} = 2, \; n_{down} = 1$.

With the tool of parton distribution functions we can factorize the total cross section into a sum of hard cross sections between different parton pairs described by perturbation theory. And the PDFs model the soft physics of the exchange, the resulting cross section looks like this:

$$\sigma = \sum_{partons \; i_1, i_2} \int_0^1 dx_1 \int_0^1 dx_2 f_{i_1}(x_1, \mu_F) f_{i_2}(x_2, \mu_F) \sigma_{hard}(p_{i_1}, p_{i_2} \to \{p_f\}) \tag{2.18}$$

2.6 Monte Carlo Integration

In computer aided calculations integrations are often performed numerically. One of the possible algorithms, frequently used in particle physics, is called Monte Carlo integration. A easy to understand introduction on the topic can be found in this publication by S. Weinzierl [11] . A similar notation to that in the paper is used in this section.

In classical numerical integration, the function f, that is to be integrated, is evaluated based on an equally spaced grid. This method can introduce a lot of unwanted correlations, especially if the domain of the function is not a cube. The easy fix, used in Monte Carlo integration, is drawing the evaluation points randomly from the integration volume V. The principle is illustrated in the following formula:

$$\int_V d^d x \; f(x) = \lim_{N\to\infty} \frac{V}{N} \sum_{n=1}^{N} f(x_n) \tag{2.19}$$

With x_n being random points in the integration volume V that are uniformly distributed. The estimated error of this approximation is proportional to $V/\sqrt{N}$. So if we double our integration volume, we have to quadruple the number of points to obtain the same relative accuracy. This makes the method badly convergent for high dimensional integrals like we encounter in particle physics.

The performance of the Monte Carlo integration can be improved if non-uniformly distributed numbers are used. If the probability distribution of the random numbers is changed from $1/V$ in the uniform case to $p(x)$ the previous equation looks like this:

$$\int_V d^d x \; f(x) = \lim_{N\to\infty} \frac{1}{N} \sum_{n=1}^{N} \frac{f(x_n)}{p(x_n)} \tag{2.20}$$

Here the probability distribution appears as a weight for the evaluated point that counteracts the effect of drawing unequally from different parts of the volume V. The variance of the summation is now governed by $f(x)/p(x)$ instead of $p(x)$. The ideal choice for the random number distribution is now of course $p(x) = f(x)/[\int_V d^d \; f(x)]$. This tells us, that in order to minimize the variance we should draw random numbers with a distribution that estimates the shape of the function we want to integrate. This method of improving the convergence of Monte Carlo integrations is called importance sampling.

3. Numerical Calculation

As a central part of the diploma thesis two Higgs-Strahlung processes were added to the monte carlo program VBFNLO [3] . In this chapter the details and challenges of this implementation are explained. First, the program VBFNLO and some of its features are introduced. Then an overview of of the aforementioned interactions is given. After that the technical details of LO and NLO QCD calculations are discussed. At the end of the chapter the phase space generation and its optimization are described along with some other minor technical peculiarities.

3.1 VBFNLO

The program derives its name from its focus on simulating vector boson fusion processes at NLO QCD accuracy. But the program has grown over the years to describe many more hadron collider interactions such as gluon fusion and diboson production. With the addition of the processes of this thesis it will include all main Higgs production channels depicted in 2.1 .

Although VBFNLO is mainly a SM program, some BSM phenomena, like anomalous Higgs couplings for example, are realized for selected processes. It is very flexible and almost all parameters of the SM can be chosen freely. VBFNLO then automatically calculates all dependent quantities like particle masses and widths, coupling constants and branching ratios.

The bulk of the program is implemented in the Fortran programming language which was specifically designed for large scale numerical calculations. Although it was developed over 60 years ago, it is still used today in many areas where computational speed is a priority.

VBFNLO contains all essential building blocks needed to calculate and analyze partonic cross sections for hadron collision experiments. For a subset of its processes it can also be interfaced with HERWIG [12][13] to simulate showering and hadronization.

3.2 ZH and ZHj

The focus of the thesis are two hadron-hadron-collision processes as one would encounter at the LHC experiment in the form of colliding protons. They are the production of a pair consisting of a Higgs and a Z-boson and the production of the same pair accompanied by a partonic jet. For the remainder of this document, we will refer to the first interaction simply by "ZH", the second will be abbreviated with "ZHj".

In processes of that type the differential cross section consists of the soft interactions between the constituents of the hadron, described by the PDFs, and the hard interaction between one parton from each hadron, expressed in a perturbative expansion matrix element. In figure 3.1 one of the LO diagrams for each matrix element is displayed.

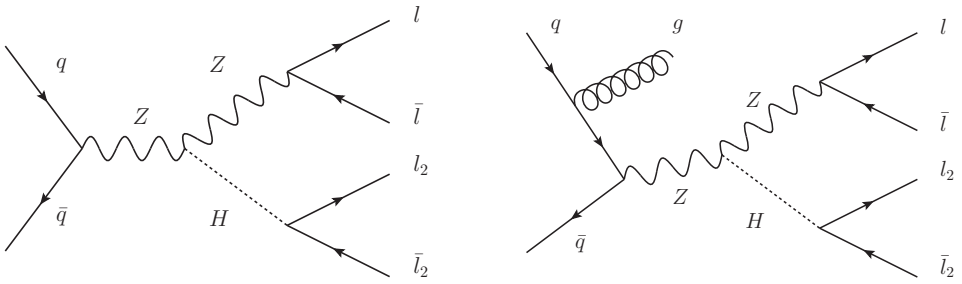

a) $p\ p \to Z\ H \to l\bar{l}\ l\bar{l}_2$ *b)* $p\ p \to Z\ H\ j \to l\bar{l}\ l\bar{l}_2\ j$

Figure 3.1: leading order diagrams.

The diagram for the first process shows a constituent quark and an antiquark producing a Z-boson. The Z-boson then radiates a Higgs boson and both of them decay into leptons afterwards. In the second process a final state gluon is radiated off the quark before the Z-boson production. This diagram interferes with the same diagram where the gluon is radiated off the antiquark at the bottom instead. For the remainder of the discussion, let the shown diagram denote the sum of both interfering diagrams.

With the above consideration in mind, all the other diagrams are obtained by repeated interchange of two of the partons in the shown diagram. This results in a total of two diagrams for ZH (from the quark and the antiquark trading places) and six non-interfering diagrams for ZHj: three diagrams for the different gluon positions multiplied by two for the placement of the remaining quarks.

None of these manipulations have any affect on the EW part of the diagrams, it stays exactly the same. In the practical implementation of the matrix elements in the program this fact is used to save computational time. For each phase space point the EW part, including the decays of the Z and Higgs boson, is only calculated once. It is stored in the form of the effective current current from the Z boson heading to the qqZ vertex. Later when the individual diagrams are computed, only the effective current coming out to the QCD part needs to be generated. Both currents are then contracted and and multiplied by the appropriate coupling resulting in the matrix element contribution of that diagram. Here special care has to be taken of the fact that the Z boson couples with different strengths to left-handed and right-handed fermions.

For the programming of the QCD part of the LO matrix elements, helicity amplitude Fortran routines, already implemented within VBFNLO, were used. A mathematical description of the corresponding formalism can be found in the paper of K. Hagiwara and D. Zeppenfeld [14]. For the realization of the EW currents, existing HELAS [15] functions were utilized.

3.2.1 Decays of the Z and Higgs boson

In the base implementation of the two processes a non-decaying Higgs boson is produced. There is a switch that decides whether a real Higgs or an off shell particle accompanied by a Breit-Wigner factor is produced.

Since the Higgs is a Lorentz scalar, it is fully described by its four-momentum. Because of this, the differential cross section for a process including a Higgs decay can be factorized into the base matrix element multiplied by a decay term. This decay term is then only dependent on the type of decay and the Higgs momentum and needs to be calculated only once for each phase space point. Many of theses decay factors are available within VBFNLO, including: $H \to b\bar{b}, \gamma\gamma, \to \tau\bar{\tau}, \to \mu\bar{\mu}, \to W^+W^- \to l\nu\ l\nu$ and $H \to ZZ \to l\bar{l}\ l\bar{l}$.

For a rigorous treatment of the decay of the Higgs into quarks one would have to consider those quarks appearing as initial state particles which would spoil our seperation of QCD and EW parts. Those contributions are color-suppressed and have been neglected.

For the decay of the Z boson, a Lorentz vector, this factorization is not possible. Therefore the base matrix element always includes the decay of the Z boson to an electron-positron pair. The decay into a muon-antimuon pair is then described by same cross section because we are treating the muons as massless. Other decays for the Z boson are not implemented.

3.3 NLO Contributions

Most contributions to the NLO cross section can be derived from LO diagrams by the insertion of additional QCD particles. There is a new type of diagram that is an exception to this which will be discussed at the end of this chapter. All other NLO diagrams contain the EW part of the LO diagram in unchanged form. To make the NLO diagrams more readable, we denote the entire EW branch of a diagram by a virtual Z boson representing the effective current connected to the QCD part. This simplification is used for the remainder of this section, it is illustrated in 3.2 .

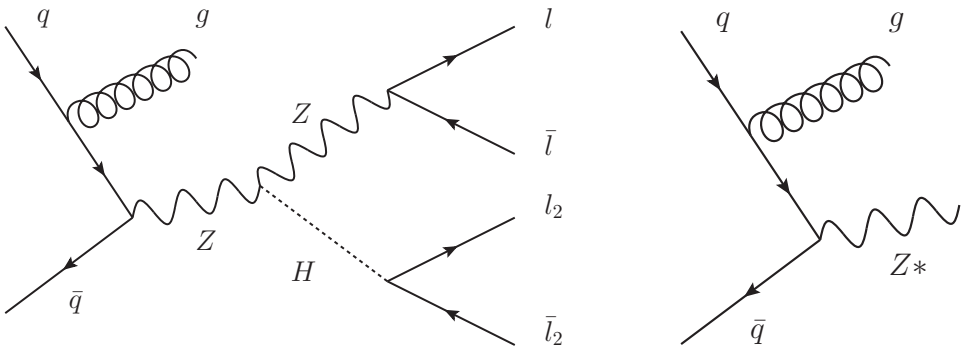

full ZHj LO diagram simplified version

Figure 3.2: Visual replacement of the EW part by a virtual Z.

3.3.1 Real Emission, Catani-Seymour-Counterterms

The real emission diagrams for the ZH process are the LO diagrams of ZHj. In figure 3.3 three characteristic real emission diagrams of the ZHj process are shown.

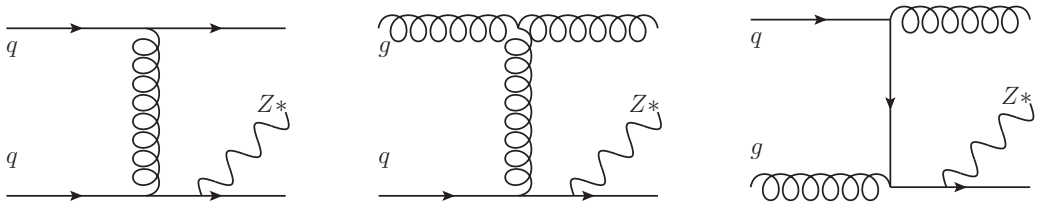

Figure 3.3: ZHj NLO real emission diagrams.

Diagrams with two gluons in the initial state constitute a sizable fraction of the total cross section since their PDF content is very high. In those diagrams top quarks, which we neglected in the initial state because of their low PDF share, could appear as final state particles. Events, in which final state top quarks are produced, can usually be distinguished from other final state flavor events in the detector. Therefore we will treat them as a separate type of process not discussed in this thesis.

As we mentioned in the theoretical introduction, these diagrams contain infrared divergencies, whenever an external parton becomes soft or a pair of external partons become collinear. In the first case there are NLO diagram in which the soft particle ($p_1 = \lambda p,\ \lambda \to 0$) is connected to another external parton (p_2) at a vertex. In that vertex the momentum of the non-soft particle is changed only by a negligible amount producing an on shell parton heading into the rest of the diagram. In the second case a diagram exists that connects both collinear particles at a vertex also producing the result of an on shell particle moving into the remainder of the diagram. Both cases can be summarized by the condition that the product of two external parton momenta approaches zero: $p_1 \cdot p_2 \to 0$. There are a finite amount of phase space regions where this criteria can be fulfilled. In the case of ZHj real emissions we have six possible pairings of the four external partons. The two initial state partons can never be soft since they produce the massive particles. And their momenta point in opposite directions so they can never be collinear. This leaves five divergent momentum constellations.

In section 2.4.3 we explained that the divergencies of the real emission cancel against the infrared singularities of the virtual corrections. This analytical cancellation poses a problem for computer calculations. Since the divergence is produced by the denominator of a propagator nearing zero we have to divide by a very small number in our differential cross section. Because of the way numbers are stored in computer calculations, small numbers are only described by a few digits of accuracy. This leads to large numerical uncertainties. Additionally, storage and handling of arbitrarily large numbers is of cause impossible but would be needed for a full description of the singularity behavior. Because of these restrictions a small lower cutoff for the momenta was implemented in the phase space generator to ensure stability of the numerical calculation.

Cancellation naturally only happens for fully inclusive cross sections. Since we also want to introduce cuts and are interested in differential cross sections over various observables, we have to introduce the cancellation at each individual phase space point manually. For this procedure counterterms are introduced that mirror the behavior of the real emission cross secton in the divergent regions. These counterterms are then subtracted from calculated matrix elements leading to finite contributions in all areas of the phase space. When we later compute the virtual corrections the counterterms are added back in canceling the infrared divergencies there. This way the total NLO cross section remains unchanged by the procedure.

To construct those counterterms, the algorithm proposed by S. Catani and M.H. Seymour [16] was followed. In the divergent regions of phase space, the real emission matrix element decouples into the vertex of the divergent pair with the attached on shell propagator and the rest of the diagram. Since the particle heading into the rest of the diagram is practically real, the two parts factorize into a singular and a finite term. The finite term is just one of the LO diagrams of the same process. This mechanic is illustrated in figure 3.4 .

This product of a LO matrix element and a term describing the divergent behavior is called a dipole. To construct the full counterterm the dipoles from all singular phase space regions are summed. The counterterm now reproduces the infrared divergence of our matrix element in all singular regions and is finite everywhere else.

For the implementation of the real emission matrix elements the same existing building blocks were used as mentioned at the end of section 3.2 . The factors for the dipole terms were also already available in VBFNLO.

3.3.2 Virtual Corrections

The virtual corrections consist of all diagrams containing a loop. For the ZHj process they appear as two types of diagrams, those were the external gluon is connected to a quark line

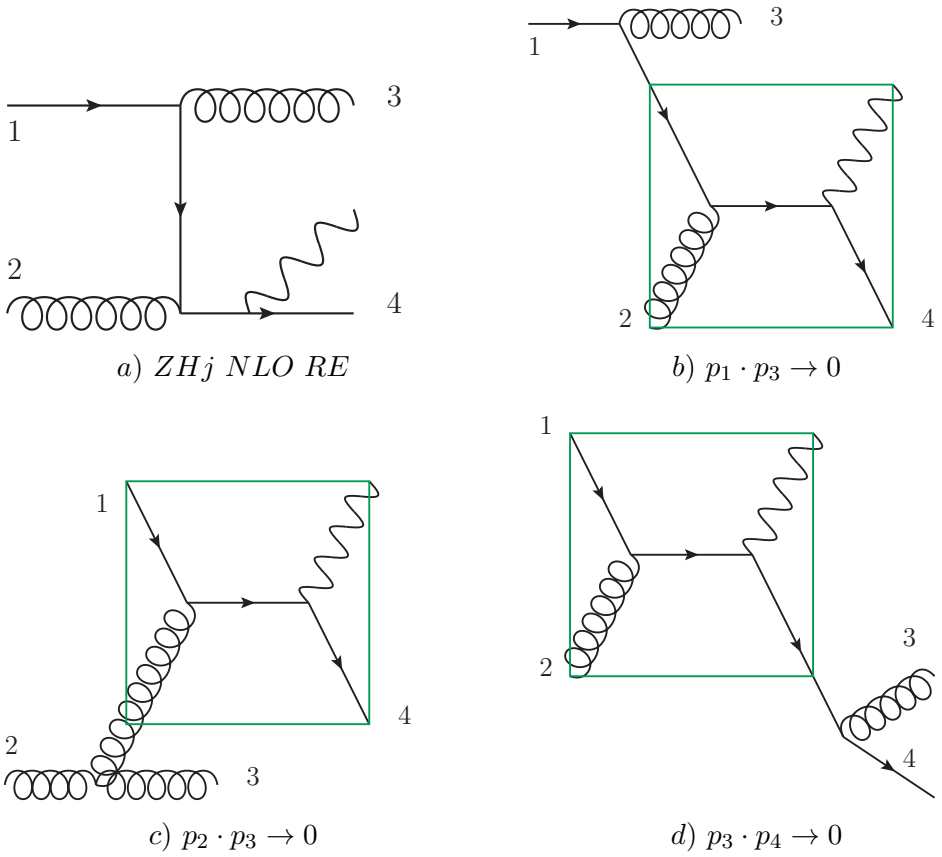

Figure 3.4: decoupling of divergent NLO real emission diagrams into singular and LO parts.

shown in figure 3.5 and those were the external gluon is connected via a tri-gluon vertex, displayed in figure 3.6 .

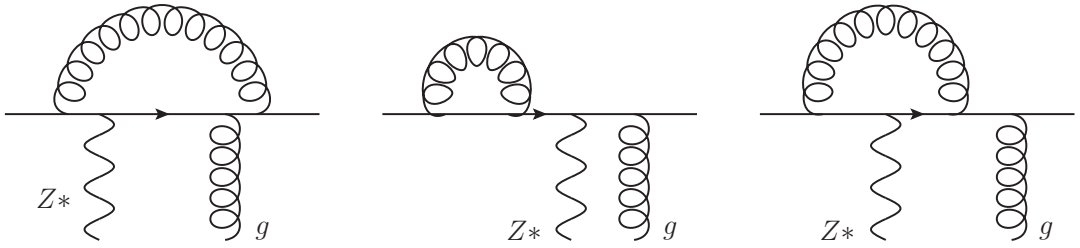

Figure 3.5: virtual diagrams from left to right: box diagram, self energy correction and vertex correction.

The first diagram shown is called a box diagram because the loop encompasses four vertices. The loop in the second diagram is a correction to a free quark propagator. In a renormalized field theory this manifests as a shift from the bare mass of the lagrangian towards the physical pole mass of the particle. The third diagram can be interpreted as a correction to the qqZ vertex it encloses.

The first three diagrams display all types of one-loop corrections to a quark line with a Z boson and a gluon attached that appear in abelian gauge theory. The pair of diagrams containing a tri-gluon represent are all additional one-loop corrections of the same quark line that appear because QCD is a non-abelian gauge theory.

Fortran routines for both of these contributions were already available in VBFNLO and were

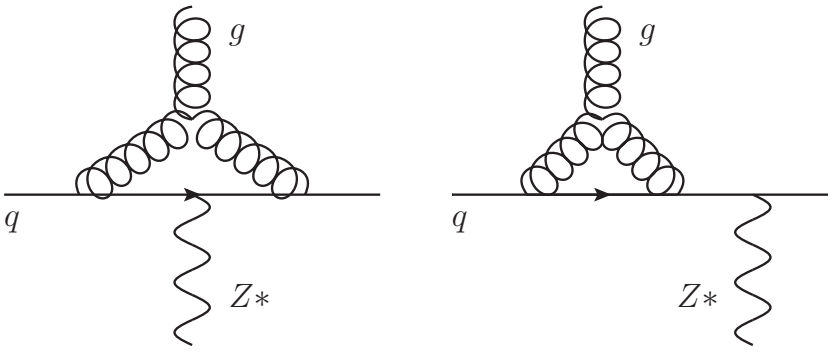

Figure 3.6: tri-gluon boxline and vertex correction diagrams.

used for the in the programming of the virtual corrections. They came with a multitude of theoretical and numerical checks to ensure the correctness of the calculation. Details about these features and the implementation of the loop routines can be found in this publication of their author F. Campanario [17] .

After the calculation of the QCD loop contributions the counterterms of the real emission have to be added to obtain a finite cross section. The real emission contains one additional final state particle compared to the virtual NLO contributions so there phase spaces do not match. To make the counterterms usable for the cancellation of the infrared loop divergencies one has to integrate out the one-parton subspace difference analytically. The whole operation is executed in the S. Catani and M.H. Seymour publication [16] . The procedure is depicted in equation 3.1 in a simplified way for m external partons in the LO cross section.

$$\sigma^{NLO} = \int_{m+1} d\sigma^R + \int_m d\sigma^V = \int_{m+1} \left[d\sigma^R - d\sigma^A \right] + \int_m d\sigma^V + \int_{m+1} d\sigma^A \tag{3.1}$$

$$= \int_{m+1} \left[d\sigma^R - d\sigma^A \right] + \int_m \left[d\sigma^V + \int_1 d\sigma^A \right] \tag{3.2}$$

Here the notation from the paper was used: $d\sigma^R$ and $d\sigma^V$ are the uncancelled real emission and virtual differential cross sections and $d\sigma^A$ are the real emission counterterms.

3.4 Phasespace Generation and Cuts

VBFNLO provides a multitude of adjustable cuts to the phase space of the integrated cross section. These can be used to simulate the limitations of the particle detector of experiments. Or they can be a tool to focus on specific regions of phase space.

In section 2.6 we already mentioned that naive monte carlo integration over high dimensional volumes converges very slowly. The phase space dimensions for hadron-hadron-collision processes only depends on the number of produced final state particles. For each final state particle we integrate over their four-dimensional momentum subspace. In addition to that we have to integrate over the two momentum fractions appearing in the PDFs. From this we can deduct all symmetries and conservation laws. All external particles being on shell reduces the total dimension by one per particle, total momentum conservation reduces four, and the rotational symmetry around the beam axis further reduces it by one. This leads to $(4-1)m + 2 - 4 - 1 = 3(m-1)$ dimensions for m final state particles. This equates to 9 phase space dimensions for ZH and 12 for ZHj at LO if we include two-particle decays for each boson.

As we already discussed, we can improve the convergence rate significantly through importance sampling. For that reason VBFNLO optimizes its phase space generator individually for each process. The most easy to predict dependence of the integrated cross section on the particle momenta at each phase space point comes from the propagators. The squared propagator of a virtual particle is proportional to $((p^2 - M^2)^2 + M^2\Gamma^2)^{-1}$, with p being the particle momentum, M the particle mass including the real part of the decay width and Γ the imaginary part of the decay width. If we normalize this resonance of the propagator we get the Breit-Wigner distribution:

$$P_{BW}(p^2) = \frac{k(M,\Gamma)}{(p^2 - M^2)^2 + M^2\Gamma^2} \tag{3.3}$$

with $k(M,\Gamma)$ being the normalization factor. If we integrate the distribution over p^2 we get the dependency of the random numbers on the momentum squared. Solving this for p^2 then tells us how to map the invariant masses of our particles to random numbers to create a Breit-Wigner resonance. The result is p^2 being created around M^2 with a tangent dependence on the drawn random numbers.

To employ this method we construct our particle momenta in a certain order. First the invariant masses of the virtual particles are constructed in the above mentioned shape. In the case of ZH and ZHj, we start with the invariant mass of the s-channel Z. It has a resonance around the sum of the masses of the Z and Higgs bosons it is connected to. The upper bound for the invariant mass is the center of mass energy of the collision. After that the invariant masses for the connected Z and Higgs boson are constructed limited through four-momentum conservation to have a combined mass less then the previous Z boson. The masses of the decay products get generated next following the same pattern. During this procedure limitations to the invariant masses through cuts are already applied. This saves time due to not generating phase space points that get discarded later anyways, and it also prevents the introduction of unwanted correlations.

The first momenta generated are those of the hadron constituents and the jets. This fixes the momentum fractions given to the PDFs and the momentum of the connected Z boson. During this procedure cuts can not be included in a natural way because they depend on the jet algorithm. So some of the generated momentum constellations have to be discarded in the end. Next, the momenta of the Z and the Higgs boson are constructed from the splitting Z boson. The direction of the momenta are generated in the rest frame of the decaying particle in spherical coordinates. The complete momenta then result from the fixed invariant masses. In this reference frame angular cut restrictions are applied. This algorithm is then repeated down the EW tree of the processes to generate all remaining momenta.

3.5 Vegas

VFBNLO uses an iterative process to optimize the distribution of random numbers given to the phase space generator. The algorithm applied is called VEGAS [18] [19] and works the following way. The goal is to find the regions in our random number space that lead to the biggest contributions to the integrated cross section when given to the phase space generator. For this purpose the d-dimensional random number space is divided into a d-dimenional grid forming bins. When random numbers are produced, they are drawn with equal probability from each of the bins and the distribution in each bin is uniform. In the first iteration all bins are of the same size resulting in an overall uniform allocation. With this distribution the integrated cross section is computed for a low number of phase space points. With the results, the bins with big contributions are made smaller leading to more

phase space points in that area during the next iteration. The integration is then performed again with higher statistics based on the new grid and the grid is readjusted based on the resulting shares of the total cross section. This way the shape of the differential cross section can be approximated for importance sampling after only a few iterations.

3.6 Flavour Scheme and Fermion Loops

With the usage of PDFs always comes the choice on how many quark flavors should be treated as massless. In the high energy regime of collider physics treating the four lightest quarks as massless is a very good and widely accepted approximation. In our calculation we decided to treat the bottom quark massless as well. With this choice, contributions to the jet cross section of all flavors except top can be calculated from the same matrix element. The PDF sets that were used for most computations were the CTEQ6L1 [20] for LO and CT10 [21] for NLO calculations.

During our calculation so far only massless fermions appeared. As a result of this no Yukawa couplings to the Higgs boson were considered. At order α_s^2, like we have for ZHj at NLO QCD, a diagram conaining a quark loop can be constructed, it is shown in 3.7 .

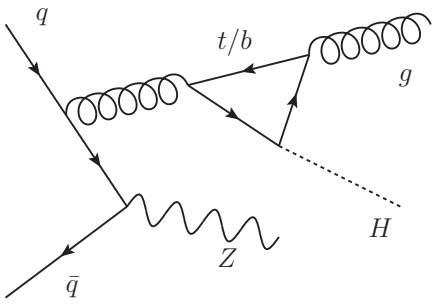

Figure 3.7: top loop diagram.

In this diagram a quark loop is connected to the quark line via a gluon. The loop can have any flavor and in the case of a top loop the Yukawa coupling to the Higgs $\frac{g}{2}\frac{m_{top}}{m_{higgs}}$ becomes relevant. The diagram was neglected based on previous results from the implementation of the very similar process $pp \to WHj$ within VBFNLO. There the inclusion of the diagram led to no significant improvement of the accuracy of the NLO calculation.

4. Checks and Comparisons

In this chapter we discuss the steps that have been taken to ensure the correctness of the calculation. A lot of internal checks have been implemented to find errors and mistakes in the calculation. Almost all of those checks can be toggled on and off, so they can be disabled once confidence is obtained that the part of the program is running correctly and calculation speed becomes important. During the implementation many working parts from other processes inside VBFNLO have been reused and adapted. This procedure safes time, avoids unnecessary mistakes and reviews older implementations.

4.1 Internal Checks

4.1.1 Tree level matrix elements

Many tree level matrix elements appear in our process implementation. They appear as LO and NLO real emission diagrams but they also appear as part of the Catani-Seymour-counterterms and as checks for the loop routines in the NLO virtual corrections. Whenever such a tree level matrix element appears as part of a process calculation, it is checked against an independent implementation of a MadGragh v4 [22] routine of the same process. It comes in handy that both MadGraph and VBFNLO decompose their matrix elements as direct sums of contributions in an orthogonal basis. Both MadGraph and VBFNLO use a helicity basis external spinors and often use the same color structures. Because of this individual spin and color constellations can be compared.

4.1.2 Cancellation of RE Divergencies

In the phasespace region, where the real emission matrix element diverges, it should be exactly discribed by the counterterm of that region. The other counterterms should be small in comparison to the two divergent terms. To ensure the cancellation is working correctly, two ratios are being checked. Firstly, the fraction of the real emission diagrams and the divergent diagram should be minus one. Secondly, the ratio of the real emission matrix element to the sum of all counterterms should be close to minus one. If this check is enabled, those values are checked for every relevant phase space point.

4.1.3 Loop Diagram Checks

The author of the loop routines also designed a multitude of checks to test the correctness of their calculations. A detailed description is given in his publication [17] . Most of the implemented checks are based on the Ward-Takeshi identity. By replacing the polarization vectors ϵ_μ of the external gluons occurring in the diagrams shown in figure 3.5 3.6 by their respective momenta k_μ the diagrams reduce to simpler terms that are proportional to leading order amplitudes. Those relations were tested against the well checked LO results.

4.2 External Checks

4.2.1 Check against Madgraph

Total cross sections have been compared with the results from the program MadGraph5 [23] . Both processes were adjusted to produce an on shell final state Higgs and the standard decay of the Z boson into a eletron-positron pair. VBFNLO derives all particle widths from model parameters whereas they are free parameters in MadGraph. For this reason the calculated widths of VBFNLO were entered in MadGraph and used for all calculations. In both programs the PDF sets CTEQ6L1 [20] for LO and CT10 [21] for NLO computations were used. Renormalization and factorization scale were set to a fixed value of the mass of the Z boson $m_Z = 91.188 MeV$. All other parameters including cuts were kept at there default MadGraph values. The results of this comparison are shown in table 4.1 .

Process	ZH		ZHj	
	LO	NLO	LO	NLO
MadGraph	18.75 ± 0.06	25.72 ± 0.07	19.27 ± 0.06	19.17 ± 0.13
VBFNLO	18.780 ± 0.008	25.694 ± 0.013	19.899 ± 0.008	19.004 ± 0.015

Table 4.1: comparison of MadGraph and VBFNLO integrated cross sections, all units in fb.

The ZHj NLO cross section shows a one percent discrepancy from the MadGraph cross section and barely misses the standard deviation range. All other cross sections are in agreement within statistical accuracy.

4.2.2 Experimental results

There are two ATLAS tech reports [24] [25] that analyze events belonging to the programmed processes. There is also this article [26] from the CMS detector discussing Higgs strahlung events in which the Z boson decays to $b\bar{b}$. None of the publications counted enough events to reconstruct a cross section so no comparison to experimental data was possible.

5. Results and Phenomenology

In this chapter some of the results generated by the programmed processes are presented and interpreted. The main focus is on the differential cross sections of various observables.

5.0.1 Renormalization Scale Dependence

The normalization scale μ_R introduced in section 2.4.3 does not correspond to an experimentally measured quantity. This additional degree of freedom is the result from only including a finite number of terms in the perturbation expansion. If the concept of perturbation theory holds, the dependence on the renormalization scale should be reduced every time we introduce a higher order term.

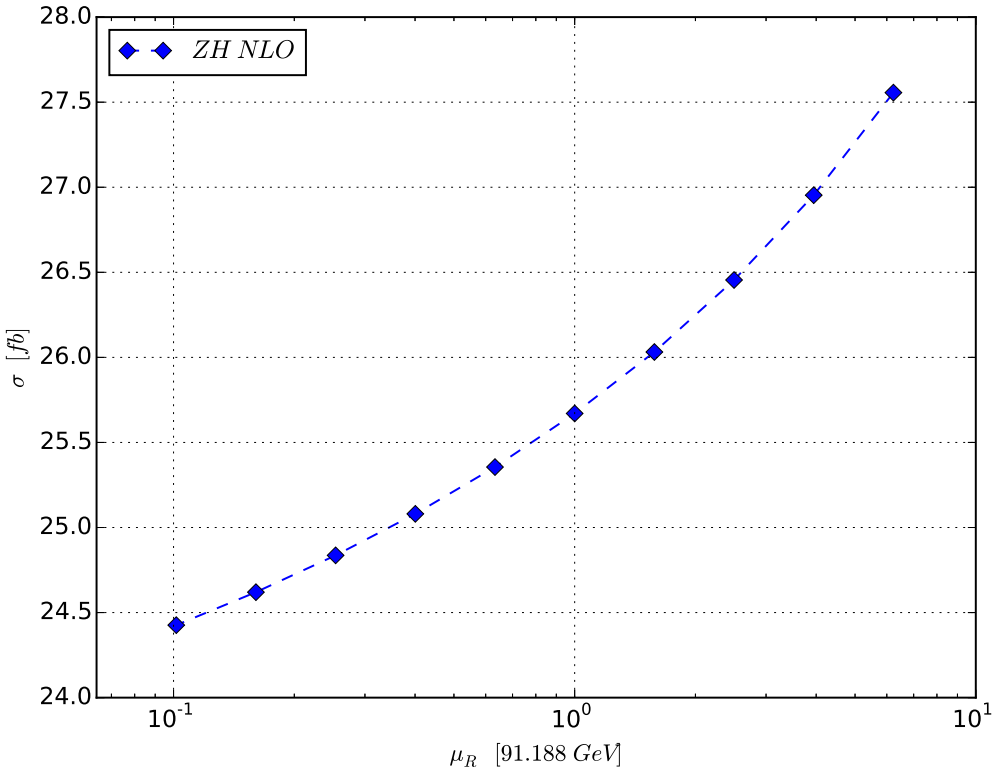

Figure 5.1: renormalization scale dependence of the ZH cross section.

The LO cross section of the ZH process does not depend on μ_R because it doesn't include a QCD coupling. In figure 5.1 the NLO cross section of the process with respect to the renormalization scale is shown. For this, μ_R was varied in a range between one tenth and ten times the Z boson mass. Although we cannot study the improvement coming from

the inclusion of higher order terms, the absolute dependence can still be used as a rough estimate of the error of the perturbation expansion. The variation of the scale by a factor of ten indroduced a change of the cross section of about 7%.

For the ZHj process a very clear attenuation of the scale dependence occurs. This result is depicted in figure 5.2 . The leading order cross section shows a heavy dependence changing by a factor of two over the investigated range of μ_R. The inclusion of NLO terms reduces this correlation to an uncertainty of about 10%.

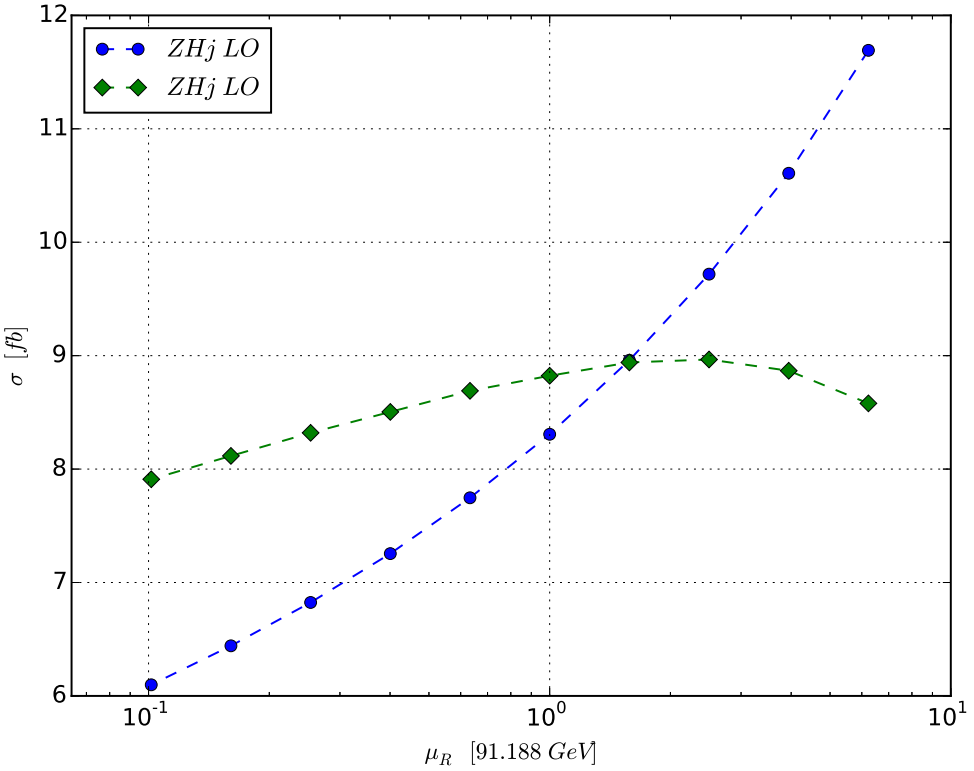

Figure 5.2: renormalization scale dependence of the ZHj cross section.

5.1 Transverse Momentum Dependence

In the analysis of scattering events an interesting observable is the transverse momentum p_T of a particle. It is the absolute value of the particle momentum perpendicular to the beam axis.

In figure 5.3 the corresponding distribution for the hardest jet of the ZHj process is shown. The dashed line shows the LO result and the solid line the differential NLO cross section. In the lower frame of the plot the the distribution of the K-factor $K = d\sigma_{NLO}/d\sigma_{LO}$ is displayed.

Clearly visible is the applied cut on the p_T of the jet at 30 GeV. The NLO cross sections mirrors the behavior of the LO result very well and the K-factor stays around the value of one. The two spikes in the NLO distribution are a result from the subraction procedure we described in section 3.3.1. The counterterms have a slightly modified momentum constellation which can move them to a different bins of the histogram then the divergence they are compensating. This effect can be seen in the contrary motion of neighboring data points and cancels out in the total cross section.

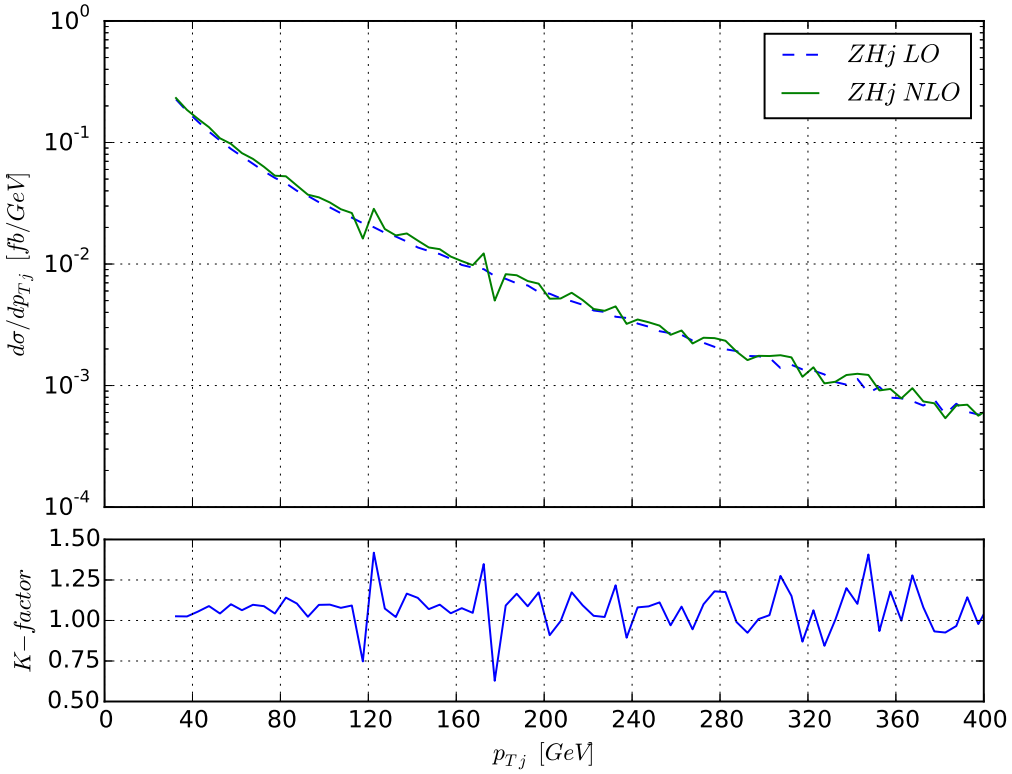

Figure 5.3: transverse momentum dependence of the hardest jet for both orders in ZHj.

In the next two figures 5.4 5.5 , the p_T dependence of the hardest lepton of each process is pictured. There were no p_T-cuts applied on those leptons which are a result of the Z boson decay. The Z boson is most frequently produced with energies around its mass because of the propagator resonance. This implies, that that it is moving relatively slowly. In its rest frame the decay leptons are therefore produced with energies around $m_Z/2 \approx 45\ GeV$. Only a portion of those leptons are produced perpendicular to the beam axis, so only part of that energy contributes to p_T. In both distributions we see a clear maximum around 50 GeV. The difference is explained by the fact we are always including the lepton with the higher p_T in the displayed distribution. This results in the peak being shifted upwards by the motion of the Z.

5.1.1 Two Jet Cross section

In figure 5.6 the differential cross sections of two jet events over the angle between the two jets ϕ_{jj} is displayed. This scenario only appears at NLO of the ZHj process. This data was produced with a cut on p_T of 30 GeV. Jets are most frequently produced in two main regions of phase space. They are either produced back-to-back, corresponding to an angle of $\phi_{jj} \approx 180°$, as shown by the peaks at either end of the figure. Or they are produced in a soft splitting, moving in the same direction. The jet algorithm cut those events out of the distribution which explains the dip in the middle of the diagram.

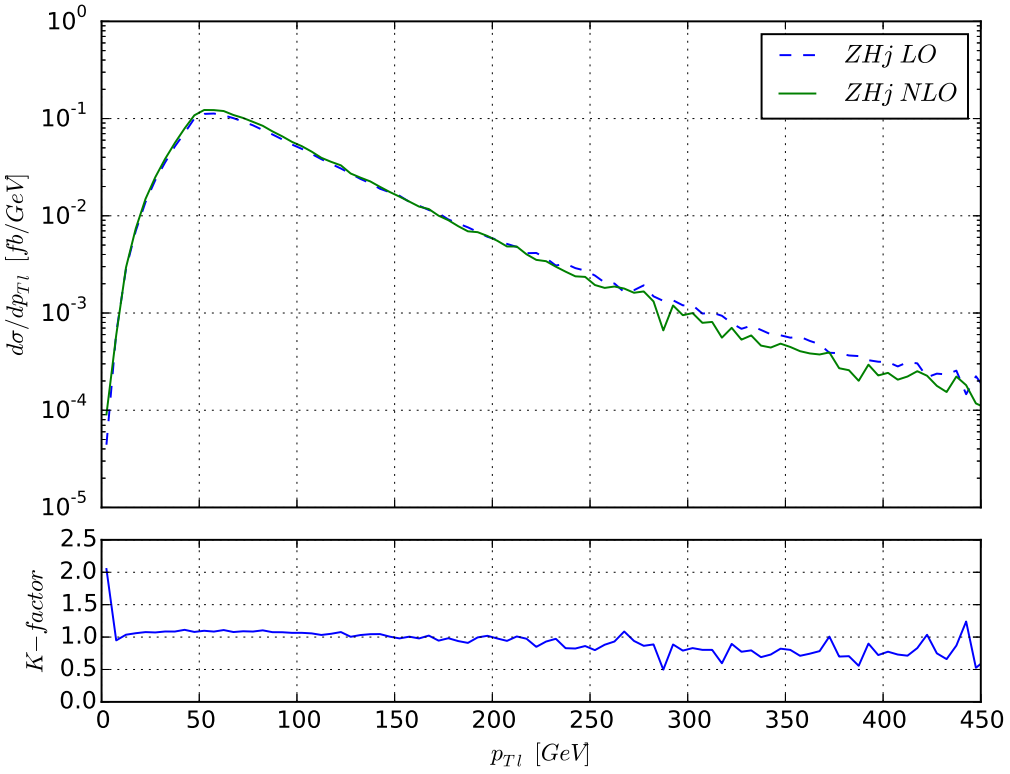

Figure 5.4: differential cross section over p_T of the hardest lepton in ZHj.

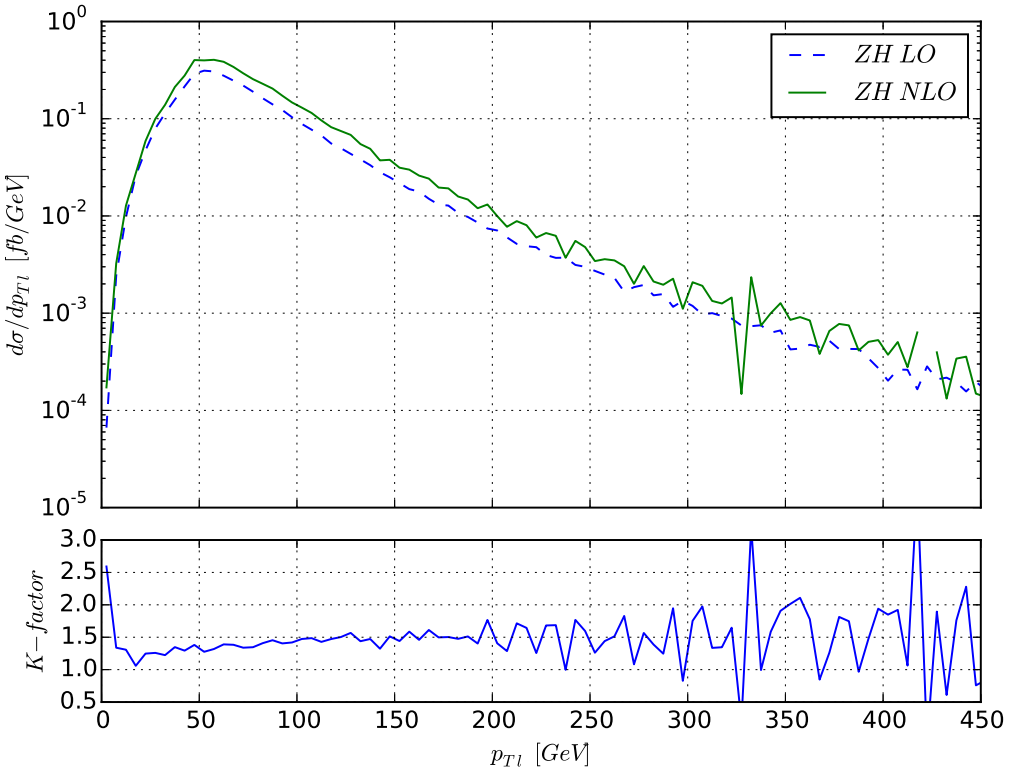

Figure 5.5: transverse momentum dependence of the hardest lepton in ZH production.

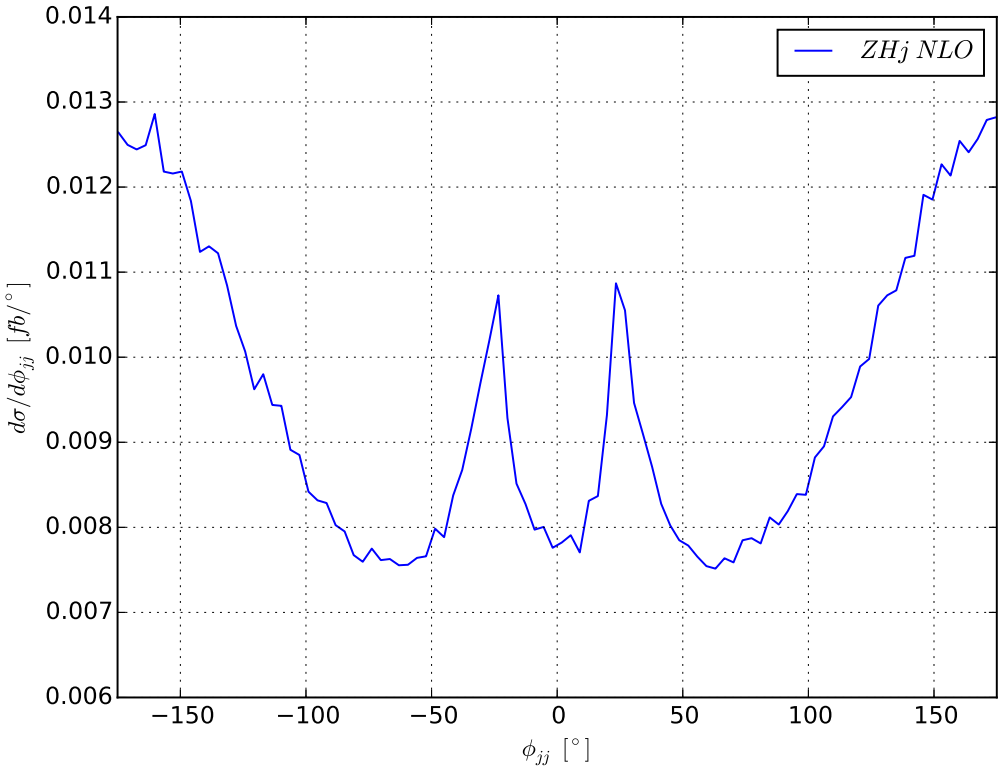

Figure 5.6: two jet differential cross section of ZHj over the angle ϕ_{jj} between the jets.

6. Summary and Outlook

The focus of this thesis was the addition of two hadron-hadron-collider processes to the program VBFNLO. To give a better understanding of the underlying mechanics, the theoretical basis of this task was briefly introduced. After that the technical details of the implementation were discussed. What followed was a short chapter about quality assurance, describing the build in checks of the program implementation. In the last chapter as regards to content a few of the produced results were displayed.

There are a few obvious extensions to the programmed processes for which I did not have the time in the end. The highest priority one is the inclusion of anomalous couplings to the Higgs boson, a beyond-SM feature that is implemented for many similar processes of the program. Another addition would be to implement the interface to HERWIG. This would make the process matrix elements available for the simulation of parton showers and hadronization.

I did not have much time to study the produced results of the simulated processes, so no real conclusion for particle searches was drawn. So at least a little bit of time in the future should be spend to analyze the generated data.

Acknowledgements

I would like to wholeheartedly thank Prof. Zeppenfeld for taking me in as a diploma student although he knew from the beginning that I might not be the most gifted physicist. He could have filled the position with a more able student but he wanted to give me the chance to finish my diploma studies. I would also like to thank him for always having an open ear for questions and for being very accommodating when problems arose.

I would like to thank Dr. Gieseke for agreeing to be the second referee of this thesis and for being a generally enjoyable person to be around at the institute.

Very special thanks go out to Robin Roth and Michael Rauch who always had time for me, when I had questions or encountered obstacles.

Thanks go out to everyone at the institute for creating a comfortable and welcoming work environment.

It goes without saying that I have unlimited gratitude for my parents who made it possible for me to study physics in the first place.

Special thanks go out to my girlfriend Heike, who supported me heavily, especially in the last few days before the submission of my thesis.

Bibliography

[1] G. Aad *et al.*, "Observation of a new particle in the search for the Standard Model Higgs boson with the ATLAS detector at the LHC," *Phys. Lett.*, vol. B716, pp. 1–29, 2012. arXiv:1207.7214.

[2] S. Chatrchyan *et al.*, "Observation of a new boson at a mass of 125 GeV with the CMS experiment at the LHC," *Phys. Lett.*, vol. B716, pp. 30–61, 2012. arXiv:1207.7235.

[3] J. Baglio *et al.*, "Release Note - VBFNLO 2.7.0," *arXiv:1404.3940*, 2014.

[4] M. Peskin and D. Schroeder, *An Introduction to Quantum Field Theory, Student Economy Edition*. Advanced Book Program, Westview Press, 2015.

[5] S. L. Glashow, "Partial-symmetries of weak interactions," *Nuclear Physics*, vol. 22, no. 4, pp. 579 – 588, 1961.

[6] S. Weinberg, "A model of leptons," *Phys. Rev. Lett.*, vol. 19, pp. 1264–1266, Nov 1967.

[7] A. Salam and J. C. Ward, "Weak and electromagnetic interactions," *Il Nuovo Cimento (1955-1965)*, vol. 11, no. 4, pp. 568–577, 1959.

[8] F. Englert and R. Brout, "Broken symmetry and the mass of gauge vector mesons," *Phys. Rev. Lett.*, vol. 13, pp. 321–323, Aug 1964.

[9] P. W. Higgs, "Broken symmetries and the masses of gauge bosons," *Phys. Rev. Lett.*, vol. 13, pp. 508–509, Oct 1964.

[10] P. W. Higgs, "Broken symmetries, massless particles and gauge fields," *Phys. Lett.*, vol. 12, pp. 132–133, 1964.

[11] S. Weinzierl, "Introduction to Monte Carlo methods," 2000. arXiv:hep-ph/0006269.

[12] M. Bahr *et al.*, "Herwig++ Physics and Manual," *Eur. Phys. J.*, vol. C58, pp. 639–707, 2008. arXiv:0803.0883.

[13] J. Bellm *et al.*, "Herwig 7.0/Herwig++ 3.0 release note," *Eur. Phys. J.*, vol. C76, no. 4, p. 196, 2016. arXiv:1512.01178.

[14] K. Hagiwara and D. Zeppenfeld, "Amplitudes for multi-parton processes involving a current at e+e-, e±p, and hadron colliders," *Nuclear Physics B*, vol. 313, no. 3, pp. 560 – 594, 1989.

[15] H. Murayama, K. Hagiwara, and I. Watanabe, "Helas: Helicity amplitude subroutines for feynman diagram evaluations," *KEK Report* 11, 1992.

[16] S. Catani and M. H. Seymour, "A General algorithm for calculating jet cross-sections in NLO QCD," *Nucl. Phys.*, vol. B485, pp. 291–419, 1997. arXiv:hep-ph/9605323.

[17] F. Campanario, "Towards pp -> VVjj at NLO QCD: Bosonic contributions to triple vector boson production plus jet," *JHEP*, vol. 10, p. 070, 2011. arXiv:1105.0920.

[18] G. P. Lepage, "VEGAS: AN ADAPTIVE MULTIDIMENSIONAL INTEGRATION PROGRAM," *Cornell Preprint*, no. CLNS-80/447, 1980.

[19] G. P. Lepage, "A new algorithm for adaptive multidimensional integration," *Journal of Computational Physics*, vol. 27, no. 2, pp. 192 – 203, 1978.

[20] J. Pumplin, D. R. Stump, J. Huston, H. L. Lai, P. M. Nadolsky, and W. K. Tung, "New generation of parton distributions with uncertainties from global QCD analysis," *JHEP*, vol. 07, p. 012, 2002. arXiv:hep-ph/0201195.

[21] H.-L. Lai, M. Guzzi, J. Huston, Z. Li, P. M. Nadolsky, J. Pumplin, and C. P. Yuan, "New parton distributions for collider physics," *Phys. Rev.*, vol. D82, p. 074024, 2010. arXiv:1007.2241.

[22] J. Alwall, P. Demin, S. de Visscher, R. Frederix, M. Herquet, F. Maltoni, T. Plehn, D. L. Rainwater, and T. Stelzer, "Madgraph/madevent v4: the new web generation," *Journal of High Energy Physics*, vol. 2007, no. 09, p. 028, 2007. arXiv:0706.2334.

[23] J. Alwall, R. Frederix, S. Frixione, V. Hirschi, F. Maltoni, O. Mattelaer, H. S. Shao, T. Stelzer, P. Torrielli, and M. Zaro, "The automated computation of tree-level and next-to-leading order differential cross sections, and their matching to parton shower simulations," *JHEP*, vol. 07, p. 079, 2014. arXiv:1405.0301.

[24] "Search for associated production of the Higgs boson in the WH-> WWW(*)-> lvlvlv and ZH-> ZWW(*)-> lllvlv channels with the ATLAS detector at the LHC," Tech. Rep. ATLAS-CONF-2013-075, CERN, Geneva, Jul 2013.

[25] "Search for new resonances decaying to a W or Z boson and a Higgs boson in the $\ell\ell b\bar{b}$, $\ell\nu b\bar{b}$, and $\nu\nu b\bar{b}$ channels in pp collisions at $\sqrt{s} = 13$ TeV with the ATLAS detector," Tech. Rep. ATLAS-CONF-2015-074, CERN, Geneva, Dec 2015.

[26] S. Chatrchyan *et al.*, "Search for the standard model Higgs boson produced in association with a W or a Z boson and decaying to bottom quarks," *Phys. Rev.*, vol. D89, no. 1, p. 012003, 2014. arXiv:1310.3687.